SCIENTIFIC REPORTS
nature research

OPEN

Chemical vs. mechanical microstructure evolution in drying colloid and polymer coatings

Thitiporn Kaewpetch[1] & James F. Gilchrist[1,2] ✉

Colloidal based films have been widely developed for a wide range of applications including chemical and electrical barrier coatings, photonic materials, biomaterials, and pharmaceutical oral drug delivery. Many previous studies investigate methods to generate uniformity or desired stratification of the final components with a desired microstructure. Few studies have been able to investigate this microstructure *in-situ* during drying. This experimental study directly tracks fluorescent colloids that are either stable in suspension or have attractive interactions during the drying process using high speed laser scanning confocal microscopy to obtain details of microstructural evolution during drying. The colloidal microstructure in stable suspensions evolves continuously during drying. Microstructures in these systems have a signature Voronoi polyhedra distribution that is defined by lognormal curve having a constant standard deviation that only depends on its chemical composition. Those formulations having strongly attractive constituents have microstructure that is heterogeneous and non-monotonic due to the mechanics associated with internal convection and capillary forces. Toward the end of drying, the influence of the mode of microstructure rearrangements remains evident.

The colloquialism "watching paint dry" is synonymous with a process that seems unchanging except over long periods of time, or pseudo-steady state. The science of drying films, both a chemical and physical process, has a long history and ubiquitous application with regard to engineering and manufacturing surfaces with desired aesthetic and barrier properties[1–8]. More recently, thin films have been designed to have advanced chemical, photonic, and electrical properties for films that behave as sensors[9–13], solar cells[14–16], and LED[17–20]. In all of these applications, a uniform or prescribed distribution of the remaining non-volatile species that make up the resulting dry film is desirable to give reliable performance. However, there often remains a large separation between formulation and prediction of final film properties.

Previous work on drying thin films aimed to characterize the physics and structure of films that display stratification, nonuniformity, partitioning, or segregation of the components. Besides stratification, skin formation, a thin solid film at the air-film interface found in drying of latex having relatively low glass transition temperature, significantly reduces drying rate[21–23]. Scanning electron microscopy, including cryo-SEM, is most commonly used for imaging dissected samples after drying is complete[24–30], though limited previous studies utilizing optical microscopy have given general information of stratification in the final film structure[31–33]. Partitioning during drying of colloidal suspensions drawn into thin films has been experimentally observed with limitations using scattering techniques[34,35] or optical coherence tomography[36] but it has predominantly been studied through simulations to understand the microstructural evolution. These studies generally concur that for stable suspensions the Péclet number, $Pe = UL/D \gg 1$ for one of the constituents leads to partitioning, where U is the velocity of the air-film interface, L is related to the colloid diameter, and D is the colloid and/or polymer diffusivity. Cracking in these films during drying through hydrodynamic stress also imparts heterogeneity in the final film structure and alters its physical, optical, and chemical properties[37–41].

What is perhaps missing from this body of literature is the microstructural evolution of the film constituents. Various approaches can be envisioned with the purpose of dictating the final structure through tuning the interparticle interactions in the formulation. In themselves, the structure of gels has received much fundamental numerical and experimental investigation to understand the relationship between structure and subtle differences in interparticle attraction[42–44]. These studies, with exceptions[45–47], largely avoid the dominating macroscopic

[1]Polymer Science and Engineering, Department of Materials Science and Engineering, Lehigh University, Bethlehem, PA, USA. [2]Department of Chemical and Biomolecular Engineering, Lehigh University, Bethlehem, PA, USA. ✉e-mail: gilchrist@lehigh.edu

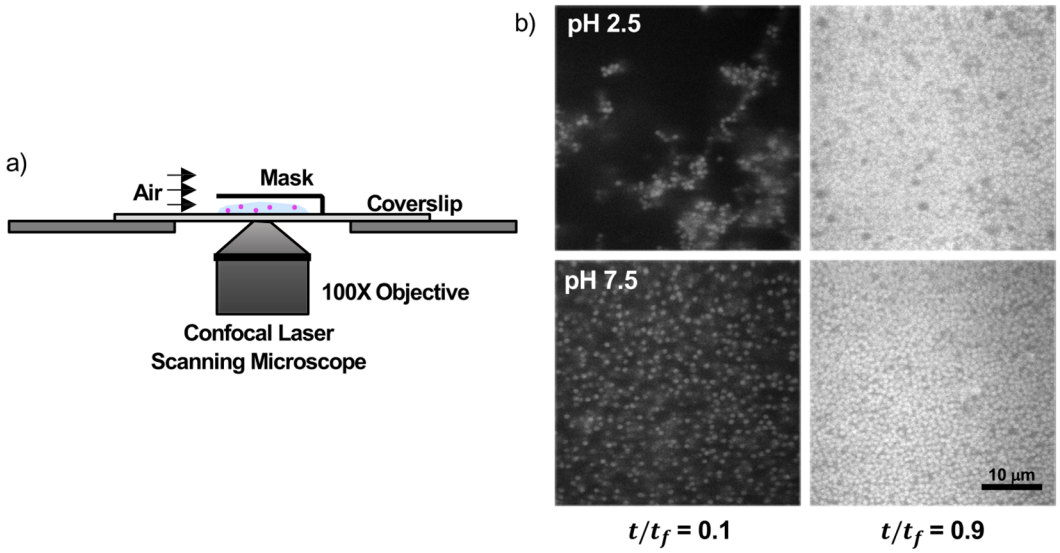

Figure 1. (**a**) Experimental setup. The blade coated sample is dried directly on the microscope under a mask that allows unidirectional drying. (**b**) Representative scans 5 μm above the substrate early and late in drying.

forces such as hydrodynamic drag from convection and capillary forces that can occur in drying films. These forces will dominate the structural evolution in drying films because surface energy will yield the gel microstructure for all systems except those at highest density and those having the strongest particle attractions, such as sintered ceramics.

This fundamental study aims to describe the key differences in the internal evolution of the microstructure between stable and strongly gelled samples. During drying of a colloid-polymer film, watching the film dry from the inside allows direct measurement of the particle microstructure during the hour-long drying process. These materials, by composition, most resemble thin films that can be used for oral drug delivery[48–51], though these are simplified versions using only the basic ingredients that make up the primary film composition. This includes aqueous solutions that have dispersed polymer, polyethylene oxide, or PEO, and silica (SiO_2) microspheres. The microspheres act as a surrogate for a hypothetical insoluble active ingredient. Citric acid is used to adjust the pH and stability of the dispersed phases. The purpose of this work is to show the differences in the evolution of microstructure in light of the inter-particle interactions.

Results

The general approach of this study is straightforward. After tuning the particle interactions of these formulations through adjustment in pH, as characterized by the solution rheology, direct imaging of the drying film was performed. The suspension contained 0.860 ± 0.020 μm core-shell synthesized fluorescent SiO_2 microspheres[52,53] with volume fraction of $\phi_0 = 0.05$ and 200,000 g/mol MW PEO solutions with weight fraction of $w_{PEO} = 0.05$ or 0.10. After pH adjustment to pH 2.5 or pH 7.5, the sample was blade coated creating a film with the initial thickness of 200 μm and then partially masked to drive drying from one direction to another, similar to continuous processing conditions (Fig. 1). Drying occurred over roughly an hour at ambient temperature of 21 °C and relative humidity of 20–50%. Below, the details for each of these steps are outlined.

Rheology of PEO and microsphere-PEO suspensions. Rheology was performed on the coating formulations prior to drying to demonstrate the effect of added SiO_2 microspheres and pH on the interaction of SiO_2 and PEO. As shown in Fig. 2, all samples have shear thinning rheology. All solutions of PEO in water at varying citric acid concentrations C_{ca} show a modest degree of shear thinning, plateauing at a constant viscosity above a shear rate $\gamma > 0.3$ 1/s. As expected, the zero shear viscosity decreases with increasing C_{ca} as the solution becomes a worse solvent for PEO.

Addition of SiO_2 microspheres into these solutions demonstrates the opposite trend in zero shear viscosity with added citric acid than that found in purely polymer solutions. At neutral conditions, addition of microspheres uniformly increases the viscosity at all shear rates by approximately 0.01 Pa·s, as is expected when there are only hydrodynamic interactions between the microspheres and PEO. This is unsurprising knowing bare SiO_2 has a moderate negative charge at neutral pH and an isoelectric point ranging from pH values of 1.5 to 3[54]. The surface charge is reduced significantly by protonation at lower pH up until its isoelectric point. Here, a pH ~2.5 corresponds to $C_{ca} = 100$ mM. Addition of citric acid for $C_{ca} \leq 1$ mM has a minor effect on the rheology. For samples where $C_{ca} \geq 10$ mM, the viscosity increases by more than an order of magnitude. This suggests a strong interaction between PEO and SiO_2, more than that of PEO responding to poor solvent quality as the pH is lowered. This adsorption is likely a result of the change in SiO_2 surface charges and the nondissociated silanol groups on SiO_2 surface hydrogen bonding with PEO. This association likely results in a heteroaggregated gel forming a network of PEO and the SiO_2 microspheres.

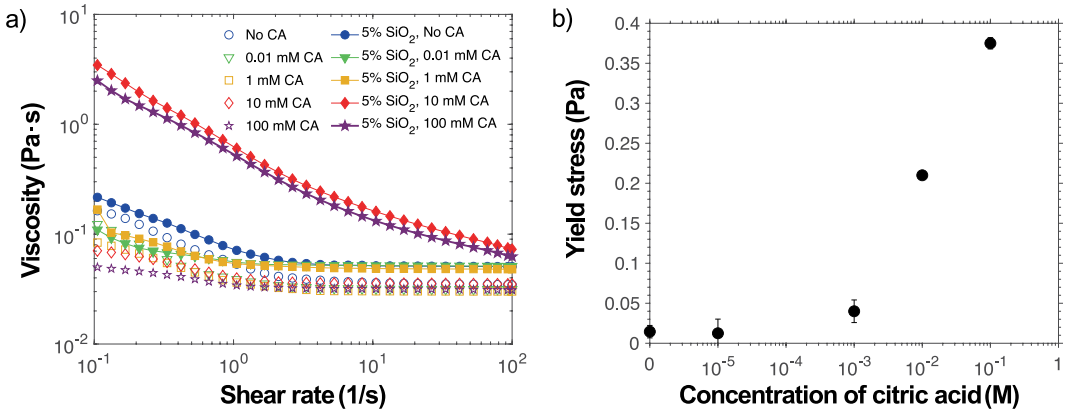

Figure 2. Rheology of the solutions including (**a**) viscosity as a function of shear rate of aqueous PEO (open symbols) and SiO_2 microsphere-PEO solutions (closed symbols) with added citric acid $0 \leq C_{ca} \leq 0.1$ M. Solutions having no added citric acid have pH of 7.5 and those at $C_{ca} = 0.1$ M have pH of 2.5. Concentrations in each sample are $w_{PEO} = 0.05$ and microsphere volume fraction of $\phi_0 = 0.05$. Yield stress of SiO_2 microsphere-PEO solutions (**b**) increases significantly with sufficient added citric acid.

In terms of formulation, besides simply increasing the viscosity, a significant yield stress forms for samples where $C_{ca} \geq 10$ mM, shown in Fig. 2b. This yield stress is also indicative of the heteroaggregated gel network. For samples at rest, this yield stress can "lock in" the microstructure resisting the effects of gravitational sedimentation and Brownian motion of particles. As evaporation occurs, densification must occur increasing the local concentration of particles due to the overwhelming strength of the capillary force from the top air-film interface.

These suspensions are coated and then partially masked to drive nearly unidirectional drying to mimic the conditions in continuous roll-to-roll oven driers as opposed to drying of sessile droplets from all edges inward. During active coating of these samples, hydrodynamic deformation of the microstructure dominates for all samples. In heteroaggregated samples, their microstructure is destroyed and reforms quickly when flow is arrested. The shear rate during coating is greater than 10^2 1/s. After the coating process is complete and drying begins, all samples show evidence of lateral drift velocity at the early stages of drying (see ESI). Thin films having significant yield stress no longer demonstrate any macroscopic flow after this initial stage while those with weak or no yield stress continue to flow due to the evaporation flux. Even though lateral flow is primarily arrested, the microstructure evolves significantly during drying.

Microstructure evolution during drying. One obvious change that occurs in thin films during drying is the evolution of concentration as solvent flux from the top surface occurs during evaporation. This has been a challenge that has only been addressed through simulations[24,55–57] and scattering experiments[34]. Through the benefit of tracking fluorescently labelled SiO_2 microspheres using high speed confocal microscopy, the evolution in concentration of microspheres, ϕ_{SiO_2}, and their microstructure can be directly determined. Figure 3 shows this transient evolution as a spatio-temporal graph. The concentration profile near the substrate is shown as a function of drying time normalized by the total time for drying up until the arrest of the microstructure, $t_f \sim 1$ h, for all samples. The sample dries further after this time without microstructure changes. The evolution of concentration presents the challenge of variation of the index of refraction over time, limiting the depth to which accurate imaging can be obtained. The depth of reduced confidence in particle location is indicated in blue. This region shows diminishing ability to see through the suspension in the early stages of drying, and then better index matching as the polymer concentration increases.

In samples at pH 7.5, a stable suspension that begins without a yield stress and lower viscosity, the evolution of the concentration profile is relatively uniform. As solvent evaporates, the top interface moves toward the substrate, as seen by the clear air-film interface and lack of any particles above this region. At the lower formulated concentration of polymer, Fig. 3a, early in the drying process only a slight inhomogeneity in concentration occurs from $0 \leq t/t_f \leq 0.6$. At $t/t_f > 0.8$, the top interface enters the observable region for this sample. Due to a difference in density of microspheres and polymer solution, the microspheres may be settling during drying. However, the maximum Péclet number for drying is $Pe_D \sim O(10)$ which is 3 order of magnitude larger than that for sedimentation, $Pe_S \sim O(10^{-2})$ (calculation is provided in the ESI). This indicates that the settling rate is slower than the advancing interface, causing the accumulation of particles near the interface. It is possible this partitioning occurs as a result of diffusiophoresis[41]. As predicted in prior studies, a higher concentration of particles, often referred to as a skin, is observed. Toward the end of this scan, some finer microstructure is observable as particle packing become denser and confined by the substrate. The particles do not crystalize with long range order, perhaps due to the presence of polymer and eventual particle destabilization as the concentration of polymer increases. Figure 3b shows a similar trend with less apparent gravitational settling due to the increased viscosity. This sample does not allow visualization of the top interface due to a greater degree of polymer resulting in a thicker final layer as the film completes drying. Within this viewable region, over many individual experiments, the resulting

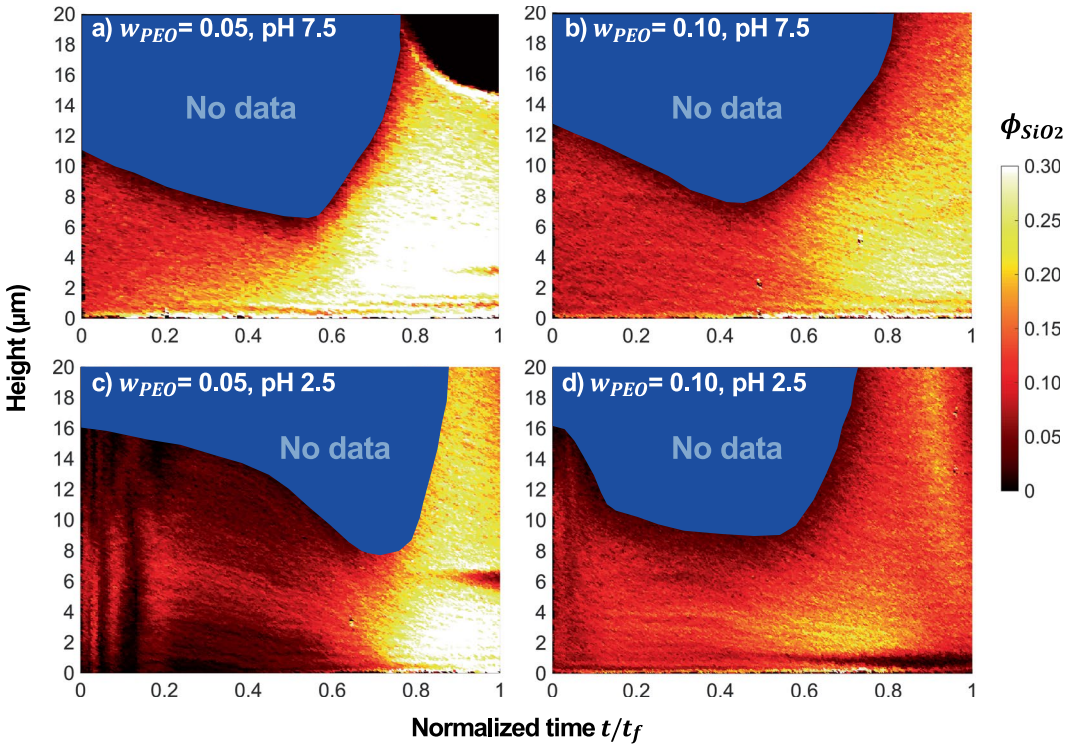

Figure 3. Concentration profile of SiO_2 microspheres in SiO_2-PEO mixtures as a function of normalized drying time t/t_f. The mixture has initial SiO_2 volume fraction $\phi_0 = 0.05$ and PEO weight fraction (**a**) $w_{PEO} = 0.05$ at pH 7.5, (**b**) $w_{PEO} = 0.10$ at pH 7.5, (**c**) $w_{PEO} = 0.05$ at pH 2.5, and (**d**) $w_{PEO} = 0.10$ at pH 2.5. Height indicates a distance from the substrate. A change in SiO_2 volume fraction, ϕ_{SiO_2}, during drying is represented as a colour scale. The depth of reduced confidence in particle location due to a mismatch of refractive index is indicated in blue.

concentration is relatively homogenous. Inhomogeneity likely occurs over much larger length scales from the internal capillary-driven flow and certainly near edges of the film.

In samples at pH 2.5 where the film initially has a significant yield stress and higher viscosity from the SiO_2-polymer heteroaggregation prior to drying, the space-time plot shows significant heterogeneity during drying. The profiles of samples shown are representative of several trials, each showing its own unique concentration evolution. In Fig. 3c, large variations of local concentration are observable at the beginning of drying. This results of large structural rearrangements of gel undergoing deformation from capillary-driven flow. Between $0.6 \leq t/t_f \leq 0.8$, a relatively sudden increase in concentration occurs as the interface provides enough mechanical strength to compress the microstructure. After this point, the microsphere distribution is relatively uniform with the exception of local phase separation due to the internal stress developed in the drying film, seen at 6 μm at the end of this scan. Figure 3d, where the film also starts with a yield stress and the polymer concentration is double that of Fig. 3c, shows similar microstructural rearrangements early in the drying process. The final density of this film is not as high as other samples as the polymer fills in the voids of the remaining microsphere-polymer heteroaggregated microstructure.

To highlight the apparent difference in microstructure evolution, Fig. 4a,b shows 3D rendered images for films having initial concentration $w_{PEO} = 0.05$ and pH 7.5 and 2.5 taken from movies of the microstructure evolution, included as Electronic Supplemental Material (ESI). Note these renderings are obtained from the experimentally determined particle locations from laser scanning confocal microscopy. From the very beginning of drying the microstructure is starkly different. At pH 7.5, microspheres are mostly uniformly distributed throughout the volume scanned and increase in density. At pH 2.5, the structure varies drastically in the early stages of drying. As noted in the concentration profiles shown in Fig. 3, uniformity dominates microstructures for both pH samples for $t/t_f > 0.8$, yet the microstructure for pH 2.5 is more open reflecting the lower average density of microstructures toward the end of drying.

The true advantage of having precise particle locations of the microspheres in these experiments is the ability to go beyond simply rendering the microstructure to demonstrate the statistical data underlying this microstructure, similar to that provided by simulations. A common tool for showing microstructural differences in suspensions is calculating the radial distribution function, g(r), as shown in Fig. 4c,d. At pH 7.5, there is no SiO_2-PEO heteroaggregation and SiO_2 microspheres are stabilized by their surface charge. The radial distribution function is relatively flat for $t/t_f \leq 0.3$. Through increasing density during drying, particles at higher concentration demonstrate a peak at $r/2a = 1$ as is common in particle suspensions. This first peak in the microsphere structure also may result from depletion interactions induced from the concentrated polymer as drying proceeds. The small changes in g(r) occur gradually through drying. At pH 2.5, the gel that gives the initial static yield stress

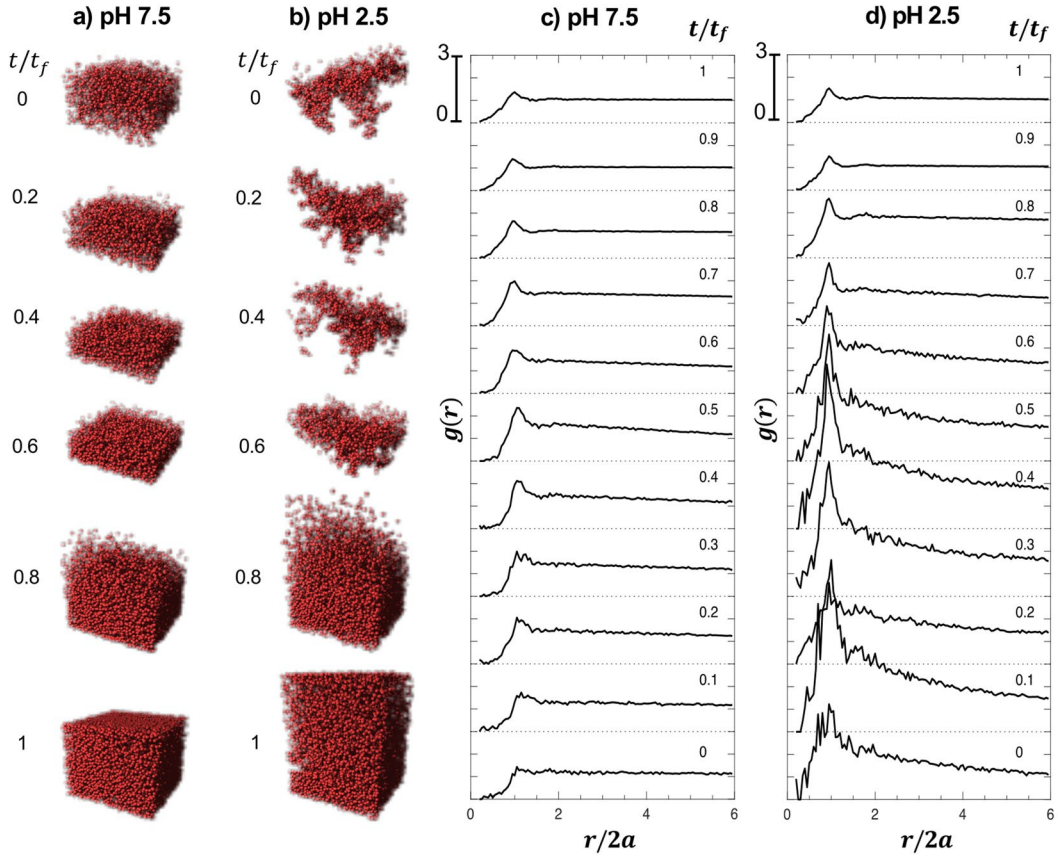

Figure 4. Rendered microstructure of observed particles through the drying process for (**a**) pH 7.5 and (**b**) pH 2.5 at arbitrary t/t_f. The average spatial distribution of particles is indicated as radial distribution function, g(r), during drying suspensions of $\phi_0 = 0.05$ and $w_{PEO} = 0.05$ at (**c**) pH 7.5 and (**d**) pH 2.5, as a function of normalized separation distance r/2a, where a is a particle radius.

of this suspension results in attractions clearly shown in a broad peak at r/2a = 1. The broadness of this peak for $t/t_f \leq 0.6$ results both from lower statistics associated with fewer particles in this open network, but also from the strong heteroaggregated gel[58]. Moreover, a long-range g(r) gradually approaches 1 from $2 < r/2a < 6$ referring to the formation of open fractal structures[59]. For $0.6 < t/t_f < 0.8$, the microspheres rapidly approach a density that results in a compact structure due to the evaporation and capillary compression from the interface, leading to the clear g(r) peak at r/2a = 1. This microstructure change occurs suddenly and relatively late in the drying process.

The g(r) gives the average spatial distribution of particles without much detail regarding the particle-level heterogeneity. Unlike g(r) where the nearest neighbour is found pair-wise, the number of neighbours in contact, $N_{contact}$, is used to determine the number of microspheres that are locally forming the network attached to a given particle (Fig. 5). As is done in prior figures, a common comparison between representative samples at pH 7.5 and pH 2.5 highlights the effect of attraction in the microstructure of these films during drying. The probability distribution of nearest neighbours is given from black to white through red.

At pH 7.5, repulsive interactions between SiO_2 particles lead to a low $N_{contact}$ when $t/t_f \leq 0.5$ (Fig. 5a,b). $N_{contact}$ still varies from 0 to 2 particles because of the random distribution of microspheres within the liquid, increasing as the microsphere density increases during drying. This distribution stays low until approximately half way through drying. For the $w_{PEO} = 0.05$ the average increases to approximately 4 particles with a wide distribution. This increase may signal the point of destabilization of the microspheres. For $w_{PEO} = 0.10$, the $N_{contact}$ also increases and its distribution broadens later in drying, but plateaus with an average of approximately 2. It is perhaps the high polymer concentration and viscosity that arrests the motion of microspheres. In contrast, at pH 2.5 particles are arrested in contact at the beginning of the experiment. $N_{contact}$ has an average of 3 microspheres and a large distribution ranging from 1 to 6 particles for $t/t_f \leq 0.5$ (Fig. 5c,d). The dynamic rearrangement of the gel is apparent from the drastic fluctuations in the profile as the gel breaks and reorders during drying, after which the particle rearrangements occur at a kinematically slow rate. These fluctuations are primarily a result of the microscopic sampling of different gel structures rather than the local rearrangement of the microstructure. As is clear from the movies and Fig. 4a,b, the stress on the microstructure is far from one that creates primary particles that reorganize. For these gels, $N_{contact}$ increases later in the drying profile than samples at pH 7.5.

The story told by the evolution in concentration, radial distribution function, and neighbours in contact suggests differences between microstructure of liquids and gels that are relatively unsurprising. As concentration increases, particles gradually come together. Upon closer inspection, this process is not gradual for gel samples

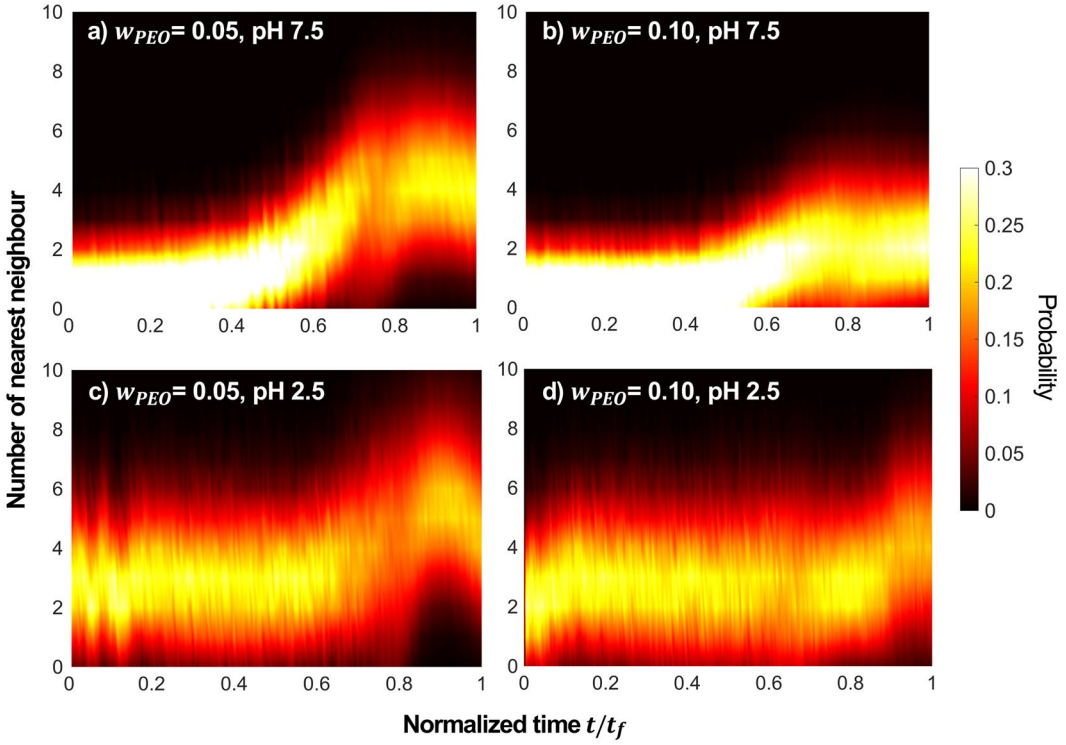

Figure 5. Distribution of neighbours in contact, $N_{contact}$, of SiO_2 during drying. The samples were prepared at $\phi_0 = 0.05$ and (**a**) $w_{PEO} = 0.05$ at pH 7.5, (**b**) $w_{PEO} = 0.10$ at pH 7.5, (**c**) $w_{PEO} = 0.05$ at pH 2.5, and (**d**) $w_{PEO} = 0.10$ at pH 2.5. Probability of number of $N_{contact}$ is indicated in a colour bar.

at pH 2.5. After large fluctuations in microstructure because of internal flow and large-scale heterogeneity, the structure is relatively unchanged for a large part of the drying process, here apparent from roughly $0.2 \leq t/t_f \leq 0.7$.

The signature of this relatively abrupt change in microstructure is highlighted in the Voronoi volume distribution shown in Fig. 6. The Voronoi volume, $\boldsymbol{V}_{v,norm}$, for a given particle is the equivalent space closer to that particle than any other particles. It is normalized by the volume for each particle in a FCC maximum packing density of same sized microspheres, or $V_{FCC} = 4a^3\sqrt{2}$. Each inset in Fig. 6a–d represents the same data plotted as a log-linear plot to highlight the tail of the distribution. Each Voronoi distribution can be fitted to a lognormal distribution[60,61]

$$P = \frac{\alpha}{V_{v,norm}\sigma\sqrt{2\pi}} \exp\left(-\frac{(\ln(V_{v,norm}) - \mu)^2}{2\sigma^2}\right),$$

where μ and σ are the lognormal distribution mean and standard deviation, respectively. The magnitude, α, is used as a fitting parameter recognizing the experimental data cannot have a distribution that spans to infinity. The mean and standard deviations for these curves are plotted as a function of time in Fig. 6e,f.

In a general drying process, the distribution of $V_{v,norm}$ is broad at $t/t_f = 0$ and becomes narrower at $t/t_f = 1$. Also, the distribution peak shifts from a larger to a smaller $V_{v,norm}$ toward the limit of $V_{v,norm} = 1$ when $t/t_f \rightarrow 1$. For $w_{PEO} = 0.05$ and $w_{PEO} = 0.10$ at pH 7.5, this transition is continuous and monotonic as drying proceeds. In terms of their lognormal distributions, while the mean decreases monotonically, the standard deviation is constant and the same for both experiments throughout drying. This suggests that at each time during the experiment, the structure is similar to what would be expected if a sample was synthesized with those components with apparently no dependence on the history of drying. For this reason, we refer to microstructure evolution in stable suspensions solely as a "chemical process" where the structure is independent of the drying profile and only depends on the local concentration.

In contrast, those samples at pH 2.5 show non-monotonic evolution in their $V_{v,norm}$ distribution. In Fig. 6e,f this discontinuous evolution is apparent. On examination of the fitted curves to these profiles, μ and σ are non-monotonic. This non-monotonic behavior suggests the microstructural rearrangements are largely a mechanical process of yielding and rearrangement. In Fig. 6f, for most of the time during drying σ is much larger for pH 2.5 than pH 7.5 where the particles have attractive interactions resulting in a larger degree of structural heterogeneity. This varying distribution in σ is much more apparent in the lower viscosity systems having initial $w_{PEO} = 0.05$ than for $w_{PEO} = 0.10$. It is unclear whether it is a result of the capillary number, $Ca = \eta U/\gamma$, having larger value for higher degree of polymer loading, therefore resisting the effects of surface tension in rearranging the microstructure or if the interactions between particles are different for different polymer concentrations.

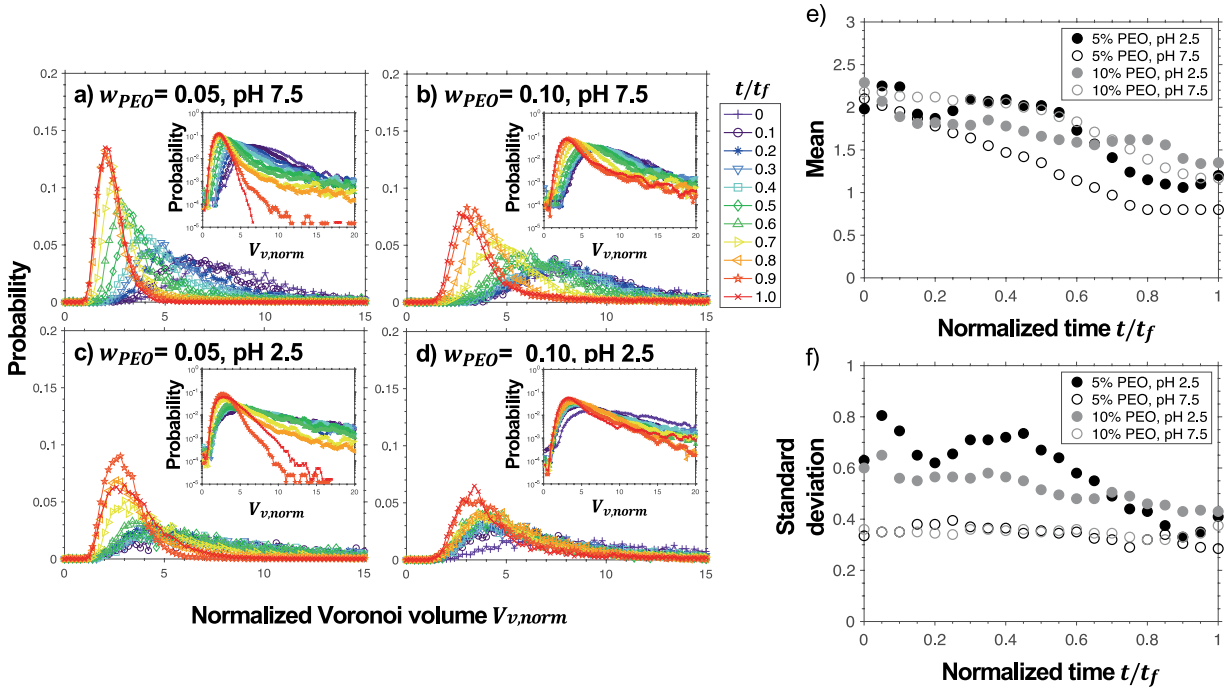

Figure 6. Normalized Voronoi volume, $V_{v,norm}$, distribution of SiO_2 in the SiO_2-PEO mixtures while drying, $0 < t/t_f < 1$. The mixtures consist of $\phi_0 = 0.05$ and (**a**) $w_{PEO} = 0.05$ at pH 7.5, (**b**) $w_{PEO} = 0.10$ at pH 7.5, (**c**) $w_{PEO} = 0.05$ at pH 2.5, and (**d**) $w_{PEO} = 0.10$ at pH 2.5. Insets show the same data plotted as a log-linear plot which is best fitted with lognormal distribution function, giving fitting parameters (**e**) mean, μ, and (**f**) standard deviation, σ, as a function of normalized drying time t/t_f.

Conclusions

While there are limitations in this approach, the data shown here definitively demonstrates two drastically different modes of microstructural rearrangements that depend on the particle-particle interactions that can be generalized past pH-dependent interactions. In designing films with engineered microstructures, a chemical route where the microstructure emulates that of a relatively isotropic distribution of particles gives a more predictable path. Alternatively, attractive particle-particle interactions set a microstructure that is immobilized at the smallest length scales for longer into the drying process until mechanical stresses dominate. This may be advantageous depending on the desired optical/mechanical/electromagnetic properties that depend on percolation or other microstructural characteristics. Clearly, challenges remain in balancing capillary forces, drying rate and internal microstructural stresses to engineer well-behaved systems. As an approach for predicting these behaviours, the capability offered in *in-situ* monitoring of the evolving microstructure will not be easily surpassed by simulations nor sacrificial techniques used previously.

Methods

Rheological measurements. Non-fluorescent SiO_2 microspheres (Fuso Chemical Co, Japan) with 0.951 ± 0.022 μm diameter and 1.8 g/cm^3 density were dispersed in a solution of Poly(ethylene oxide) or PEO (Colorcon®) with molecular weight of 200,000 g/mol and approximate density of 1.1 g/cm^3 [62] to obtain the suspension of initial SiO_2 volume fraction $\phi_0 = 0$ or 0.05, and PEO weight fraction $w_{PEO} = 0.05$. Before performing the rheological measurements, pH of the samples was adjusted. Viscosity and yield stress were determined using an Ares 2000 ex rheometer (TA Instruments) with a 0.29° 60 mm cone and plate geometry. Both viscosity and yield stress measurements were performed using a steady shear stress sweep method at 25 °C and within a shear rate range of 0.1 to 100 1/s.

2D and 3D microstructure evolution imaging. Core-shell Rhodamine B fluorescent SiO_2 microspheres were synthesized following established protocols[52,53] and characterized by using scanning electron microscopy. The synthesized fluorescent microsphere has a diameter of 0.860 ± 0.02 μm and approximate particle density of 1.8 g/cm^3. The rhodamine B dye has an absorption wavelength of 543 nm and an emission wavelength of 580 nm. The dispersion of the fluorescent labelled microspheres in a 200,000 g/mol MW PEO solution were formulated at $\phi_0 = 0.05$ and $w_{PEO} = 0.05$ or 0.10. All formulations were adjusted to pH 2.5 or pH 7.5 before performing the experiment. The sample was blade-coated on a glass substrate and dried unidirectionally at ambient temperature of 21 °C and relative humidity of 20–50%. The initial film thickness is roughly 200 μm. The film microstructure was visualized in both two and three dimensions using high speed laser scanning confocal microscopy (Vteye, Visitech International) with a laser wavelength of 488 nm with a 510 long pass filter at 72 fps within 30 s time interval until a drying process completed. Total drying time was roughly 1–2 hours. Due to mismatch of refractive

index, n, between silica microspheres ($n_{SiO_2} = 1.42$) and PEO solutions ($n_{PEO} = 1.45$ and $n_{water} = 1.33$), the depth of confidence in particle location is limited, indicated in blue in Fig. 3.

Image analysis. Location of fluorescent SiO_2 microspheres in 2D and 3D scans were analysed using particle tracking algorithms developed by Crocker and Grier[63] and additional 3D particle tracking algorithms provided by Professor Eric Weeks. A bandpass filter was applied before particle locations were identified from the brightest particle centroids[63]. From 2D scans, mean square displacement (MSD) was analyzed and correlated to particle diffusivity[64,65]. In case of 3D scans, a concentration profile of the SiO_2 microspheres was generated from tracked positions as a function of normalized drying time t/t_f. An algorithm of 3D radial distribution function, g(r), was used to obtain the g(r) analysis at different drying times. Distribution of neighbours in contact were also generated by an algorithm provided by Professor Eric Weeks. Noted that a maximum bond length parameter, b_{max}, in the code is different for the sample at pH 2.5 ($b_{max} = 1.3$) and pH 7.5 ($b_{max} = 1.1$) due to the existence of PEO absorption on microsphere surface. Lastly, three-dimension Voronoi volume analysis was performed[66].

Received: 14 April 2020; Accepted: 28 May 2020;
Published online: 24 June 2020

References

1. Wyart, F. B. & Daillant, J. Drying of solids wetted by thin liquid films. *Can. J. Phys.* **68**, 1084–1088 (1990).
2. Routh, A. F. Drying of thin colloidal films. *Rep. Prog. Phys.* **76**, 046603 (2013).
3. Vrentas, J. S. & Vrentas, C. M. Drying of solvent-coated polymer films. *J. Polym. Sci. Part B Polym. Phys.* **32**, 187–194 (1994).
4. Sheetz, D. P. Formation of films by drying of latex. *J. Appl. Polym. Sci.* **9**, 3759–3773 (1965).
5. Keddie, J. L. Film formation of latex. *Mater. Sci. Eng. R Reports* **21**, 101–170 (1997).
6. Routh, A. F. & Russel, W. B. Horizontal drying fronts during solvent evaporation from latex films. *AIChE J.* **44**, 2088–2098 (1998).
7. Overbeek, A. Polymer heterogeneity in waterborne coatings. *J. Coatings Technol. Res.* **7**, 1–21 (2010).
8. de Gans, B.-J. & Schubert, U. S. Inkjet printing of well-defined polymer dots and arrays. *Langmuir* **20**, 7789–7793 (2004).
9. Xi, Q., Chen, X., Evans, D. G. & Yang, W. Gold nanoparticle-embedded porous graphene thin films fabricated via layer-by-layer self-assembly and subsequent Thermal annealing for electrochemical sensing. *Langmuir* **28**, 9885–9892 (2012).
10. Ozaydin-Ince, G., Coclite, A. M. & Gleason, K. K. CVD of polymeric thin films: applications in sensors, biotechnology, microelectronics/organic electronics, microfluidics, MEMS, composites and membranes. *Rep. Prog. Phys.* **75**, 016501 (2012).
11. Chen, X. *et al*. Thin-film formation of imidazolium-based conjugated polydiacetylenes and their application for sensing anionic surfactants. *Angew. Chemie Int. Ed.* **49**, 1422–1425 (2010).
12. Liu, H. *et al*. Physically flexible, rapid-response gas sensor based on Colloidal quantum dot solids. *Adv. Mater.* **26**, 2718–2724 (2014).
13. Xu, H., Wu, P., Zhu, C., Elbaz, A. & Gu, Z. Z. Photonic crystal for gas sensing. *J. Mater. Chem. C* **1**, 6087–6098 (2013).
14. Pawar, S. M. *et al*. Single step electrosynthesis of Cu2ZnSnS4 (CZTS) thin films for solar cell application. *Electrochim. Acta* **55**, 4057–4061 (2010).
15. Wang, W., Wu, S., Reinhardt, K., Lu, Y. & Chen, S. Broadband light absorption enhancement in thin-Film silicon solar cells. *Nano Lett.* **10**, 2012–2018 (2010).
16. Pillai, S. & Green, M. A. Plasmonics for photovoltaic applications. *Sol. Energy Mater. Sol. Cells* **94**, 1481–1486 (2010).
17. Lee, S. H., Park, S. Y. & Lee, K. J. Laser lift-off of GaN thin film and its application to the flexible light emitting diodes. *Proc. SPIE* **8460**, 846011 (2012).
18. Wen, S.-Y. *et al*. A novel integrated structure of thin film GaN LED with ultra-low thermal resistance. *Opt. Express* **22**, A601–A606 (2014).
19. Ding, Q.-A., Li, K., Kong, F., Zhao, J. & Yue, Q. Improving the vertical light extraction efficiency of GaN-based thin-film flip-chip LED with double embedded photonic crystals. *IEEE J. Quantum Electron.* **51**, 1–9 (2015).
20. Um, J. G. *et al*. Active-matrix GaN μ-LED display using oxide thin-film transistor backplane and flip chip LED bonding. *Adv. Electron. Mater.* **5**, 1800617 (2019).
21. Carter, F. T., Kowalczyk, R. M., Millichamp, I., Chainey, M. & Keddie, J. L. Correlating particle deformation with water concentration profiles during Latex film formation: reasons that softer Latex films take longer to dry. *Langmuir* **30**, 9672–9681 (2014).
22. König, A. M., Weerakkody, T. G., Keddie, J. L. & Johannsmann, D. Heterogeneous drying of colloidal polymer films: dependence on added salt. *Langmuir* **24**, 7580–7589 (2008).
23. Gorce, J.-P. *et al*. Vertical water distribution during the drying of polymer films cast from aqueous emulsions. *Eur. Phys. J. E* **8**, 421–429 (2002).
24. Makepeace, D. K. *et al*. Stratification in binary colloidal polymer films: experiment and simulations. *Soft Matter* **13**, 6969–6980 (2017).
25. Trueman, R. E. *et al*. Autostratification in drying colloidal dispersions: experimental investigations. *Langmuir* **28**, 3420–3428 (2012).
26. Atmuri, A. K., Bhatia, S. R. & Routh, A. F. Autostratification in drying colloidal dispersions: effect of particle interactions. *Langmuir* **28**, 2652–2658 (2012).
27. Luo, H., Scriven, L. E. & Francis, L. F. Cryo-SEM studies of latex/ceramic nanoparticle coating microstructure development. *J. Colloid Interface Sci.* **316**, 500–509 (2007).
28. Zhou, J., Man, X., Jiang, Y. & Doi, M. Structure formation in soft-matter solutions induced by solvent evaporation. *Adv. Mater.* **29**, 1703769 (2017).
29. Cardinal, C. M., Jung, Y. D., Ahn, K. H. & Francis, L. F. Drying regime maps for particulate coatings. *AIChE J.* **56**, 2769–2780 (2010).
30. Ma, Y., Davis, H. T. & Scriven, L. E. Microstructure development in drying latex coatings. *Prog. Org. Coatings* **52**, 46–62 (2005).
31. Grillet, A.-C. *et al*. Control of the morphology of waterborne nanocomposite films. *Polym. Int.* **53**, 569–575 (2004).
32. Prolongo, S. G., Moriche, R., Sánchez, M. & Ureña, A. Self-stratifying and orientation of exfoliated few-layer graphene nanoplatelets in epoxy composites. *Compos. Sci. Technol.* **85**, 136–141 (2013).
33. Basheva, E. S., Danov, K. D. & Kralchevsky, P. A. Experimental study of particle structuring in vertical stratifying films from Latex suspensions. *Langmuir* **13**, 4342–4348 (1997).
34. Kim, S., Hyun, K., Struth, B., Ahn, K. H. & Clasen, C. Structural development of nanoparticle dispersion during drying in polymer nanocomposite films. *Macromolecules* **49**, 9068–9079 (2016).
35. Boulogne, F. *et al*. Structural anisotropy of directionally dried colloids. *Europhys. Lett.* **105**, 38005 (2014).
36. Huang, H. *et al*. Integrating optical coherence tomography with gravimetric and video analysis (OCT-Gravimetry-Video method) for studying the drying process of polystyrene latex system. *Sci. Rep.* **8**, 12962 (2018).
37. Singh, K. B. & Tirumkudulu, M. S. Cracking in drying colloidal films. *Phys. Rev. Lett.* **98**, 218302 (2007).
38. Singh, K. B., Bhosale, L. R. & Tirumkudulu, M. S. Cracking in drying colloidal films of flocculated dispersions. *Langmuir* **25**, 4284–4287 (2009).
39. Tirumkudulu, M. S. & Russel, W. B. Cracking in drying Latex films. *Langmuir* **21**, 4938–4948 (2005).

40. Sekido, T. *et al*. Effects of pH on the structure and mechanical properties of dried pH-responsive latex particles. *Soft Matter* **13**, 7562–7570 (2017).
41. Sear, R. P. & Warren, P. B. Diffusiophoresis in nonadsorbing polymer solutions: The Asakura-Oosawa model and stratification in drying films. *Phys. Rev. E* **96**, 062602 (2017).
42. Dickinson, E. Structure and rheology of simulated gels formed from aggregated olloidal particles. *J. Colloid Interface Sci.* **225**, 2–15 (2000).
43. Dickinson, E. Structure and rheology of colloidal particle gels: insight from computer simulation. *Adv. Colloid Interface Sci.* **199–200**, 114–127 (2013).
44. Puertas, A. M., Fuchs, M. & Cates, M. E. Comparative simulation study of colloidal gels and glasses. *Phys. Rev. Lett.* **88**, 098301 (2002).
45. Furukawa, A. & Tanaka, H. Key role of hydrodynamic interactions in colloidal gelation. *Phys. Rev. Lett.* **104**, 245702 (2010).
46. Varga, Z., Wang, G. & Swan, J. The hydrodynamics of colloidal gelation. *Soft Matter* **11**, 9009–9019 (2015).
47. Varga, Z. & Swan, J. Hydrodynamic interactions enhance gelation in dispersions of colloids with short-ranged attraction and long-ranged repulsion. *Soft Matter* **12**, 7670–7681 (2016).
48. Kunte, S. & Tandale, P. Fast dissolving strips: a novel approach for the delivery of verapamil. *J. Pharm. Bioallied Sci.* **2**, 325–328 (2010).
49. Susarla, R. *et al*. Fast drying of biocompatible polymer films loaded with poorly water-soluble drug nano-particles via low temperature forced convection. *Int. J. Pharm.* **455**, 93–103 (2013).
50. Crowley, M. M. *et al*. The influence of guaifenesin and ketoprofen on the properties of hot-melt extruded polyethylene oxide films. *Eur. J. Pharm. Sci.* **22**, 409–418 (2004).
51. Prodduturi, S., Manek, R. V., Kolling, W. M., Stodghill, S. P. & Repka, M. A. Solid-state stability and characterization of hot-melt extruded Poly(ethylene oxide) films. *J. Pharm. Sci.* **94**, 2232–2245 (2005).
52. Van Blaaderen, A. & Vrij, A. Synthesis and Characterization of Colloidal Dispersions of Fluorescent, Monodisperse Silica Spheres. *Langmuir* **8**, 2921–2931 (1992).
53. Verhaegh, N. A. M. & Van Blaaderen, A. Dispersions of Rhodamine-Labeled Silica Spheres: Synthesis, Characterization, and Fluorescence Confocal Scanning Laser Microscopy. *Langmuir* **10**, 1427–1438 (1994).
54. Kosmulski, M. *Chemical properties of material surfaces*. (Marcel Dekker, 2001).
55. Howard, M. P., Nikoubashman, A. & Panagiotopoulos, A. Z. Stratification in drying polymer–polymer and colloid–polymer mixtures. *Langmuir* **33**, 11390–11398 (2017).
56. Cheng, S. & Grest, G. S. Dispersing nanoparticles in a polymer film via solvent evaporation. *ACS Macro Lett.* **5**, 694–698 (2016).
57. Howard, M. P., Nikoubashman, A. & Panagiotopoulos, A. Z. Stratification dynamics in drying colloidal mixtures. *Langmuir* **33**, 3685–3693 (2017).
58. Kohl, M., Capellmann, R. F., Laurati, M., Egelhaaf, S. U. & Schmiedeberg, M. Directed percolation identified as equilibrium pre-transition towards non-equilibrium arrested gel states. *Nat. Commun.* **7**, 11817 (2016).
59. Dinsmore, A. D., Weeks, E. R., Prasad, V., Levitt, A. C. & Weitz, D. A. Three-dimensional confocal microscopy of colloids. *Appl. Opt.* **40**, 4152–4159 (2001).
60. Starr, F. W., Sastry, S., Douglas, J. F. & Glotzer, S. C. What do we learn from the local geometry of glass-forming liquids? *Phys. Rev. Lett.* **89**, 125501 (2002).
61. Kumar, S., Kurtz, S. K., Banavar, J. R. & Sharma, M. G. Properties of a three-dimensional poisson-Voronoi tesselation: a Monte Carlo study. *J. Stat. Phys.* **67**, 523–551 (1992).
62. Gonzalez-Tello, P., Camacho, F., Blazquez, G., Gonzllez-Tello, P. & Bllzquez, G. Density and viscosity of concentrated aqueous solutions of polyethylene glycol. *J. Chem. Eng. Data* **39**, 611–614 (1994).
63. Crocker, J. C. & Grier, D. G. Methods of digital video microscopy for colloidal studies. *J. Colloid Interface Sci.* **179**, 298–310 (1996).
64. Mason, T. G. Estimating the viscoelastic moduli of complex fluids using the generalized Stokes-Einstein equation. *Rheol. Acta* **39**, 371–378 (2000).
65. Wehrman, M. D., Lindberg, S. & Schultz, K. M. Multiple particle tracking microrheology measured using bi-disperse probe diameters. *Soft Matter* **14**, 5811–5820 (2018).
66. Hyongju, P. The function calculates arbitrary polytope bounded Voronoi diagram. https://github.com/hyongju/Polytope-bounded-Voronoi-diagram.

Acknowledgements

Data analysis was performed using algorithms code developed by Crocker and Grier[63] and code developed by using the tutorial and additional algorithms provided by Professor Eric Weeks (http://www.physics.emory.edu/faculty/weeks//idl/). TK was supported by the Royal Thai Scholarship. This material is based upon work supported by the National Science Foundation under Grant No. 1936541. The authors appreciate insight and feedback provided by R.K. Prud'homme, Princeton University.

Author contributions

T.K. performed all experiments and data analysis. Both authors wrote and reviewed the manuscript.

Competing interests

The authors declare no competing interests.

Additional information

Supplementary information is available for this paper at https://doi.org/10.1038/s41598-020-66875-0.

Correspondence and requests for materials should be addressed to J.F.G.

Reprints and permissions information is available at www.nature.com/reprints.

Publisher's note Springer Nature remains neutral with regard to jurisdictional claims in published maps and institutional affiliations.